

# Contrast-Source-Based Physics-Driven Neural Network for Inverse Scattering Problems

Yutong Du<sup>1</sup> and Zicheng Liu<sup>1</sup>

<sup>1</sup>Department of Electronic Engineering, School of Electronics and Information, Northwestern Polytechnical University, Xi'an 710029, China

January 28, 2026

## Abstract

Deep neural networks (DNNs) have recently been applied to inverse scattering problems (ISPs) due to their strong nonlinear mapping capabilities. However, supervised DNN solvers require large-scale datasets, which limits their generalization in practical applications. Untrained neural networks (UNNs) address this issue by updating weights from measured electric fields and prior physical knowledge, but existing UNN solvers suffer from long inference time. To overcome these limitations, this paper proposes a contrast-source-based physics-driven neural network (CSPDNN), which predicts the induced current distribution to improve efficiency and incorporates an adaptive total variation loss for robust reconstruction under varying contrast and noise conditions. The improved imaging performance is validated through comprehensive numerical simulations and experimental data.

## 1 Introduction

Electromagnetic inverse scattering imaging [1] is a technique that reconstructs the material and structure of targets from the measured scattered fields. The applications of inverse scattering imaging include non-destructive testing[2], airport security screening[3], and subsurface inspection[4]. The challenges of the inverse problems are the nonlinearity caused by multiple scattering effects, and the ill-posedness caused by limited measurement data and propagation loss. The design target of inversion algorithms is to enable accurate, stable, and fast imaging.

Due to the lack of large and diverse real measurement datasets, data-driven deep learning methods[5; 6; 7; 8; 9; 10] inherently suffer from limited generalization in practical applications. This motivates the use of untrained neural networks in ISPs [11; 12; 13] with high flexibility and no need for training data. Song et al.[11] proposed a uSOM-Net to alternately update the induced current and contrast with physical losses defined from both the data and the state equations. Du et al.[13] proposed a physics-driven

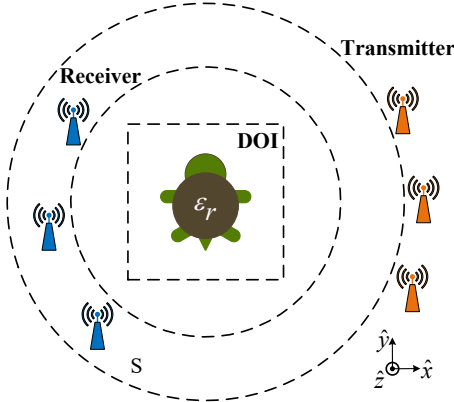


Figure 1: The configuration of 2-D inverse scattering problems.

neural network (PDNN) solver to leverage the governing physical laws to guide the updating of network hyperparameters to ensure physics-consistent solutions, and apply morphological processing to identify subregions containing true scatterers, thereby reducing the computational burden. However, uSOM cannot accurately reconstructs targets with complex structures. PDNN updates the relative permittivity iteratively, requiring scattered field computations at each step. Even with sub-region selection, the computational speed is still not fast enough. Both solvers fall short of practical application requirements.

In this paper, the contrast-source-based physics-driven neural network (CSPDNN) is proposed to solve ISPs. Instead of directly estimating the relative permittivity, the neural network predicts the induced current distribution, thereby avoiding the explicit matrix inversion of PDNN and significantly improving computational efficiency. Furthermore, an adaptive weight updating strategy is introduced for the total variation (TV) regularization term in the loss function, enabling the solver to automatically adjust to different contrast levels and noise conditions. The effectiveness and robustness of the proposed solver are demonstrated through comprehensive numerical simulations and experimental validations.

## 2 Formulation of ISPs

The schematic diagram of the 2-D ISPs is shown in Figure 1, where the domain of interest (DOI) is illuminated by transverse magnetic (TM) waves from the  $N_t$  transmitters in turn. Scattered fields are collected by  $N_s$  receivers to reconstruct the electrical properties (e.g., relative permittivity, conductivity, etc.) of the DOI. The problems can be described by state and data equations. The state equation describes the coupling between the incident field and the scatterers, and the multiple scattering effects within the DOI can be expressed as [1]

$$\mathbf{E}^{\text{tot}}(\mathbf{r}) = \mathbf{E}^{\text{inc}}(\mathbf{r}) + k_0^2 \int_{\text{DOI}} g(\mathbf{r}, \mathbf{r}') \mathbf{J}(\mathbf{r}') d\mathbf{r}', \text{ for } \mathbf{r} \in \text{DOI}, \quad (1)$$

where  $\mathbf{E}^{\text{tot}}(\mathbf{r})$  and  $\mathbf{E}^{\text{inc}}(\mathbf{r})$  are the total and incident electric field at the observation point  $\mathbf{r}$  within the DOI.  $k_0$  denotes the wavenumber in free space.  $g$  is the scalar Green's function.  $\mathbf{J}$  is the induced current source, given by  $\mathbf{J}(\mathbf{r}') = \chi(\mathbf{r}') \mathbf{E}^{\text{tot}}(\mathbf{r}')$ , where  $\chi(\mathbf{r}') = \epsilon_r(\mathbf{r}') - 1$  and  $\epsilon_r(\mathbf{r}')$  is the relative permittivity.

---

**Algorithm 1** Weight Update of CSPDNN

---

- 1: Calculate  $\mathbf{G}_D$  and  $\mathbf{G}_S$ ;
- 2: Initialize network parameters  $\boldsymbol{\theta} \leftarrow \boldsymbol{\theta}_0$ ;
- 3: Construct the network input  $\mathbf{J}_{(0)} \oplus \boldsymbol{\epsilon}_{r(0)}$ ;
- 4: Update the equivalent current by CNN:  $\mathbf{J}_{\boldsymbol{\theta}} = \mathcal{F}_{\boldsymbol{\theta}}(\mathbf{J}_{(0)} \oplus \boldsymbol{\epsilon}_{r(0)})$ ;
- 5: Compute the relative permittivity distribution:  $\chi_{\boldsymbol{\theta}} = \frac{\sum_{n=1}^{N_i} \mathbf{E}_{\text{tot}, \boldsymbol{\theta}}^H \mathbf{J}_{\boldsymbol{\theta}}}{\sum_{n=1}^{N_i} \|\mathbf{E}_{\boldsymbol{\theta}}^{\text{tot}}\|^2}$ ,  $\boldsymbol{\epsilon}_{r, \boldsymbol{\theta}} = 1 + \chi_{\boldsymbol{\theta}}$ .
- 6: Update  $\boldsymbol{\theta}$  by minimizing loss function;
- 7: Output  $\boldsymbol{\epsilon}_r^{\text{pre}} = \boldsymbol{\epsilon}_{r, \boldsymbol{\theta}}$ .

---

The data equation

$$\mathbf{E}^{\text{sca}}(\mathbf{r}) = k_0^2 \int_{\text{DOI}} g(\mathbf{r}, \mathbf{r}') \mathbf{J}(\mathbf{r}') d\mathbf{r}', \text{ for } \mathbf{r} \in \mathcal{S} \quad (2)$$

quantifies the scattered fields collected by the receivers. ISPs aim to reconstruct the distribution of  $\chi$  from the measured scattered fields and prior physical knowledge of the targets. By discretizing (1) and (2), the state and data equations can be rewritten in matrix form as

$$\mathbf{E}^{\text{tot}} = \mathbf{E}^{\text{inc}} + \mathbf{G}_D \mathbf{J}, \quad (3)$$

$$\mathbf{E}^{\text{sca}} = \mathbf{G}_S \mathbf{J}. \quad (4)$$

where  $\mathbf{G}_D$  and  $\mathbf{G}_S$  denote the discretized integral operators associated with the state and data equations.

### 3 Neural Network Solver

A contrast-source-based physics-driven neural network (CSPDNN) solver is proposed to predict the distribution of the induced current. The network is trained using a composite loss function comprising state consistency, data fidelity, a lower-bound constraint, and total-variation (TV) regularization. Additionally, an adaptive mechanism is designed to dynamically adjust the weight of the TV regularization term.

#### 3.1 Inversion scheme

The inversion scheme of the proposed solver is summarized in Algorithm 1. The network input is formed by concatenating the initial induced current  $\mathbf{J}_{(0)}$  and the initial relative permittivity  $\boldsymbol{\epsilon}_{r(0)}$  estimated using the efficient ISP solver backpropagation (BP) method [14]. The network predicts an updated induced current  $\mathbf{J}_{\boldsymbol{\theta}}$ , then the corresponding relative permittivity  $\boldsymbol{\epsilon}_{r, \boldsymbol{\theta}}$  is subsequently computed. The network parameters are optimized by minimizing loss function. Finally, the predicted permittivity distribution  $\boldsymbol{\epsilon}_r^{\text{pre}}$  is obtained.

To handle complex-valued data, both the induced current and the permittivity are decomposed into their real and imaginary components, resulting in a four-channel input and a two-channel output. The proposed solver adopts a hybrid convolutional–fully connected architecture that maps an input of size

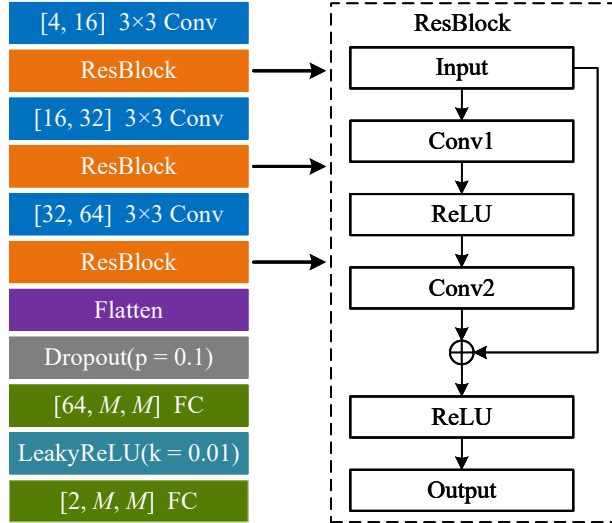


Figure 2: The network architecture of the proposed CSPDNN solver.

$M \times M$  to an output of the same spatial resolution. As shown in Figure 2, the network consists of three convolutional layers with increasing channel numbers of 16, 32, and 64, respectively. Each convolutional layer is followed by a residual block and a LeakyReLU activation to facilitate hierarchical feature extraction. The convolutional features are subsequently flattened and processed by two fully connected layers with dropout and activation functions, enabling global information integration. The batch-size is set to  $N_i$ .

### 3.2 Loss Function

The loss function applied by the CSPDNN solver is a summation of four items, *i.e.*,

$$\text{Loss} = L^{\text{State}} + L^{\text{Data}} + L^{\text{Bound}} + L^{\text{TV}}, \quad (5)$$

and the four items are defined as

$$L^{\text{State}} = \frac{\|\mathbf{J}_{\theta} - \chi_{\theta}(\mathbf{E}_{\theta}^{\text{tot}})\|^2}{\|\mathbf{E}^{\text{inc}}\|^2}, \quad (6a)$$

$$L^{\text{Data}} = \frac{\|\mathbf{E}_{\theta}^{\text{sca}} - \mathbf{E}_{\text{mea}}^{\text{sca}}\|^2}{\|\mathbf{E}_{\text{mea}}^{\text{sca}}\|^2}, \quad (6b)$$

$$L^{\text{Bound}} = \alpha \|\text{ReLU}(1 - \mathbf{R}\mathbf{e}\{\epsilon_{r,\theta}\})\|_1, \quad (6c)$$

$$L^{\text{TV}} = \beta(\Re\{\chi_{\theta}\})f(\Re\{\chi_{\theta}\}) + \beta(\Im\{\chi_{\theta}\})f(\Im\{\chi_{\theta}\}). \quad (6d)$$

where  $L^{\text{State}}$  represents the residual of the predicted induced current and the induced current computed from the estimated contrast and total field.  $L^{\text{Data}}$  quantifies the discrepancy between the measured scattered fields  $\mathbf{E}_{\text{mea}}^{\text{sca}}$  and the scattered fields corresponding to the predicted solution  $\mathbf{J}_{\theta}$ .  $L^{\text{Bound}}$  enforces a lower-bound constraint on the real part of the relative permittivity.  $L^{\text{TV}}$  is the total-variation regularization term [9], imposing smoothness on the desired solution, where  $f(v) = \sum_{i,j} \sqrt{(v^{i,j+1} - v^{i,j})^2 + (v^{i+1,j} - v^{i,j})^2}$ ,

and  $\beta(u) = \frac{\beta_0}{M(u)}$ ,  $M(\cdot)$  denotes mean operator.  $\alpha$  and  $\beta_0$  are hyperparameters set to  $1 \times 10^{-4}$  and  $1 \times 10^{-5}$ , which are found to yield stable and satisfactory performance.

### 3.3 Training settings

The solvers are trained by workstation equipped with 128-GB RAM, 3.20-GHz CPU, and NVIDIA GeForce RTX 4090 GPU. The network parameters are optimized using the Adam optimizer with an initial learning rate of  $1 \times 10^{-3}$ , which is halved every 1000 epochs. The maximum number of training epochs is set to 1500.

## 4 Numerical and Experimental Results

To evaluate the CSPDNN solver, numerical simulations are conducted on a  $0.15\text{m} \times 0.15\text{m}$  DOI, which is discretized into a  $64 \times 64$  grid. The imaging system comprises 36 transmitters and 36 receivers uniformly distributed along a circular with a radius of  $20\lambda$ , sharing the same center as the DOI. The scattered fields are generated using the method of moments (MoM)[15; 16] at 4 GHz.

### 4.1 Reconstruction of Complex Scatterers

To assess the applicable scope of the proposed CSPDNN solver, six representative cases are considered involving complex scatterer configurations, and the corresponding reconstruction results are shown in Figure 3.

For Case 1, corresponding to the classical Austria-shaped scatterer, both SOM and uSOM suffer from blurred boundaries, particularly along the ring-shaped structure. PDNN partially recovers the target geometry. However, noticeable shape distortion and locally overestimated contrast values are observed. CSPDNN produces a much sharper boundary with reconstructed values closest to the ground truth, demonstrating superior accuracy. Cases 2 and 4 involve overlapping circular scatterers with different relative permittivities, superimposed on a ring-shaped or circular background. SOM and uSOM are only able to identify the relative spatial location of the scatterers, while the reconstructed shapes are severely distorted. Although both PDNN and CSPDNN successfully recover the overall geometry and size of the scatterers, PDNN exhibits visible local overestimation of contrast in Case 2. CSPDNN achieves more uniform reconstructions with clearly defined boundaries. In Case 3, where scatterers of different sizes and contrast are distributed in the DOI, all solvers can distinguish the locations and contrast differences of the three targets. However, the small low-contrast scatterer on the left is easily misjudged as background artifacts by the results of SOM and uSOM. Both PDNN and CSPDNN yield reconstructions that are much closer to the ground truth, correctly preserving the characteristics of the small low-contrast scatterer. For Case 5, consisting of concentric circular scatterers with different radii and permittivities, SOM and uSOM tend to misjudge the outer weak scatterer as an artifact induced by the stronger inner target. PDNN achieves accurate contrast estimation but produces visibly non-smooth reconstructions. CSPDNN delivers high-quality imaging results with improved smoothness and uniformity, although the reconstructed edges

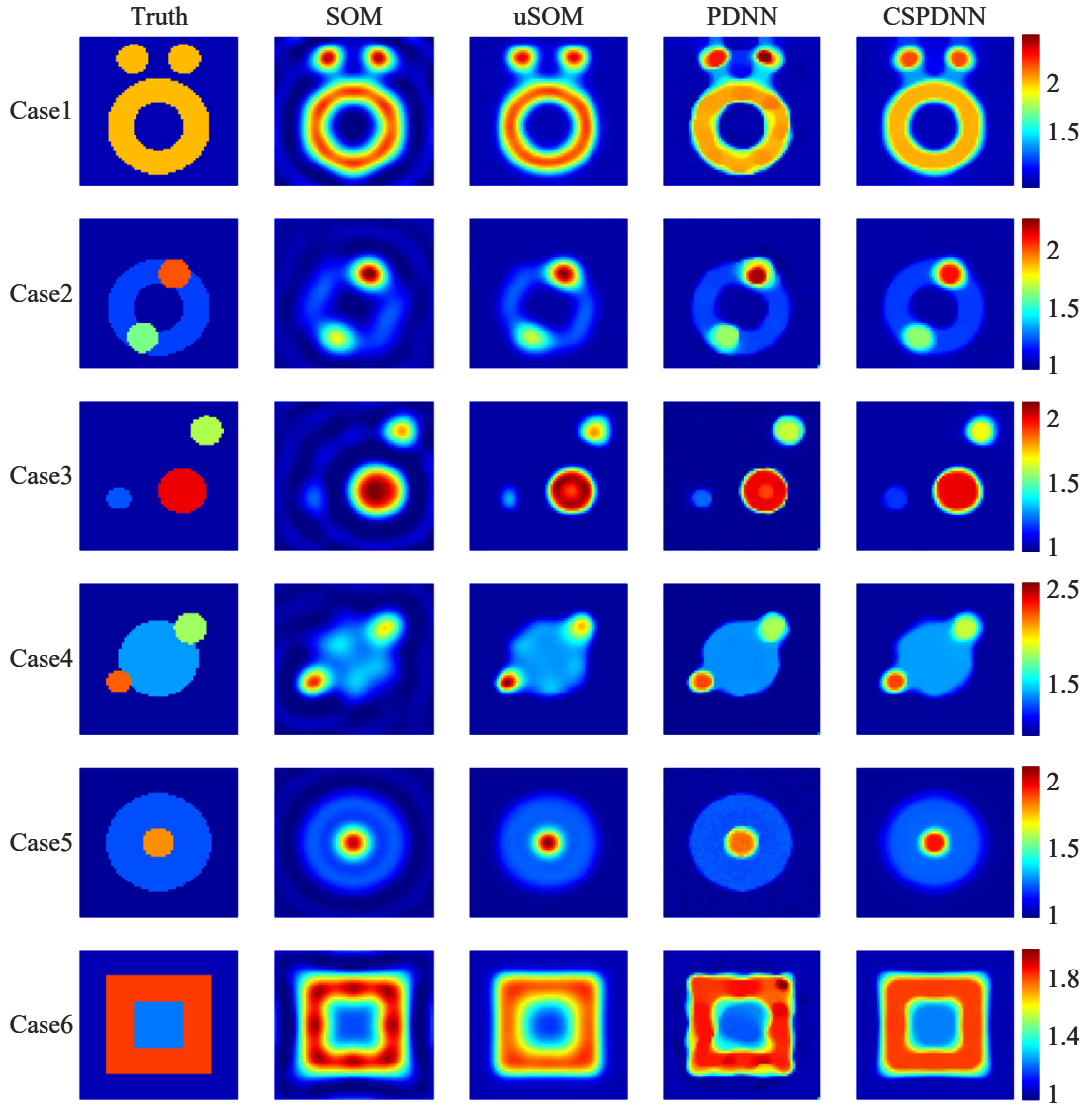


Figure 3: Comparison of imaging results for complex scatterers obtained by SOM, uSOM, PDNN, and CSPDNN solver.

remain slightly less sharp. In Case 6, involving overlapping scatterers with sharp corners, SOM, uSOM, and PDNN are unable to clearly distinguish whether the central response corresponds to a weak scatterer or an artifact induced by a strong scatterer. In contrast, CSPDNN successfully reconstructs the central weak scatterer with a uniform relative permittivity that is clearly separable from the background, yielding the most accurate reconstruction among all the considered solvers. Overall, these results demonstrate that the proposed solver achieves more accurate and physically consistent reconstructions across a wide range of challenging configurations.

In addition to reconstruction accuracy, the inference time of different solvers is also evaluated. As summarized in Table 1, CSPDNN consistently achieves the shortest inference time across all cases, requiring approximately 28s per reconstruction. Compared with the other solvers, CSPDNN provides an average speedup of approximately 3 $\times$  to 4 $\times$ . These results demonstrate that CSPDNN significantly improves

	SOM	uSOM	PDNN	CSPDNN
Case 1	98.28s	78.73s	115.36s	27.91s
Case 2	89.03s	79.40s	87.45s	28.24s
Case 3	132.9s	78.79s	72.70s	27.55s
Case 4	116.8s	80.12s	85.76s	28.87s
Case 5	120.77s	78.77s	77.76s	28.47s
Case 6	125.64s	78.84s	138.75s	27.30s

Table 1: Comparison of inference time between SOM, uSOM, PDNN and CSPDNN solver

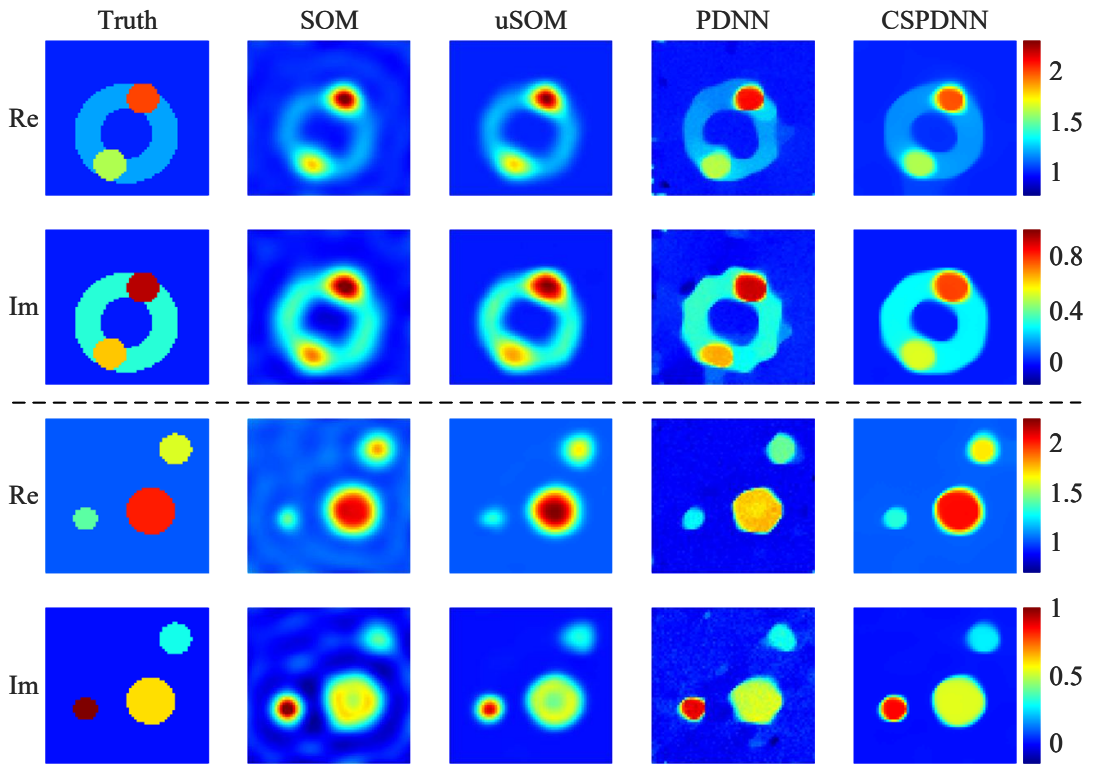


Figure 4: Reconstruction results of lossy scatterers using SOM, uSOM, PDNN, and CSPDNN solver.

inference efficiency while maintaining high reconstruction quality.

## 4.2 Reconstruction of Lossy Scatterers

This subsection further investigates more representative lossy scatterers, and two typical reconstruction results are presented in Figure 4. As seen, SOM and uSOM exhibit similar reconstruction behaviors. The ring-shaped scatterer in the first case is noticeably distorted by both solvers, although uSOM yields a cleaner background than SOM. For the first example, PDNN produces accurate contrast values but suffers from shape distortion and background noise, while in the second case it tends to underestimate

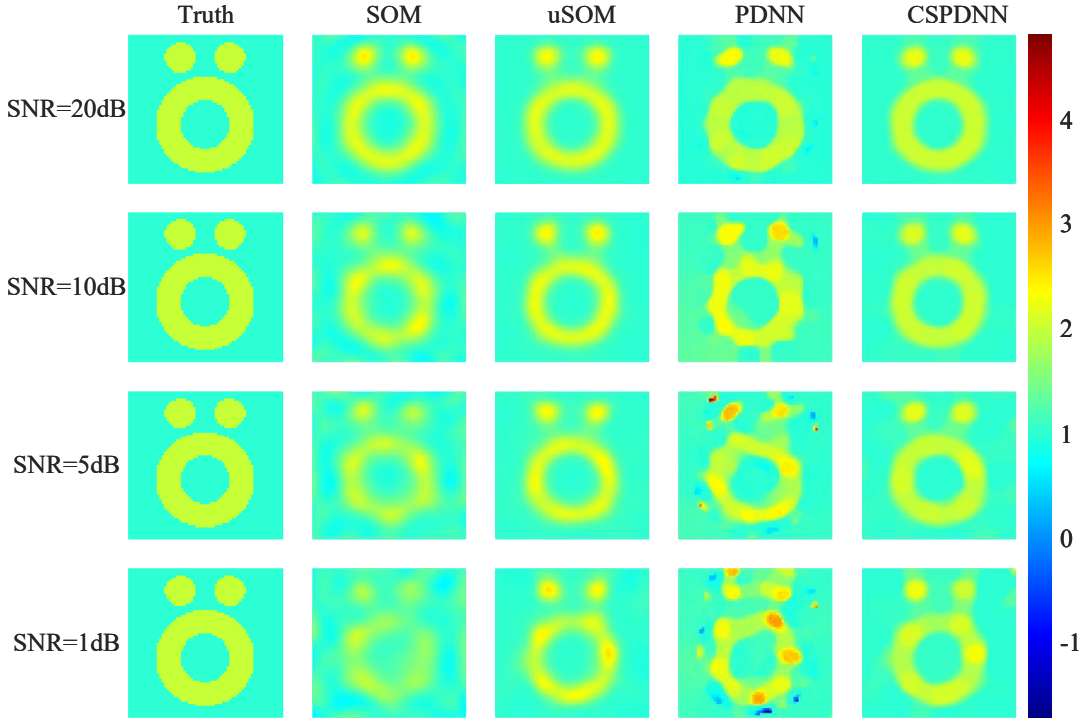


Figure 5: Tests of noise robustness of the ISP solver SOM, uSOM, PDNN and CSPDNN.

the relative permittivity. In contrast, CSPDNN delivers clean backgrounds and accurate reconstructions for both cases, demonstrating the applicability of the proposed solver in lossy scattering scenarios.

### 4.3 Influence of Noise Levels

Noise robustness is a critical consideration for ISPs. Here, the imaging performance of SOM, uSOM, PDNN, and CSPDNN is evaluated under additive white Gaussian noise with signal-to-noise ratios (SNRs) of 20, 10, 5, and 1 dB. The corresponding reconstruction results are shown in Figure 5. When  $\text{SNR} = 20$  dB, all solvers achieve satisfactory reconstructions. When the SNR decreases to 10 dB, SOM and PDNN exhibit noticeable shape distortions, whereas uSOM and CSPDNN maintain reliable reconstruction quality. Under more severe noise conditions, PDNN suffers from pronounced background artifacts that hinder shape identification. In contrast, uSOM and CSPDNN remain robust even at very low SNR, with CSPDNN providing the most accurate contrast estimation and the clearest boundary definition.

### 4.4 Experimental Validation

The imaging performance of CSPDNN is validated using the experimental dataset ‘‘FoamDielExt’’ provided by the Fresnel Institute [17]. As shown in Figure 6, PDNN exhibits a noticeable underestimation of the strong scatterer on the left side, whereas CSPDNN reconstructs this region more accurately. These results indicate that CSPDNN generalizes well to multiple-scatterer scenarios and high-contrast experimental measurements.

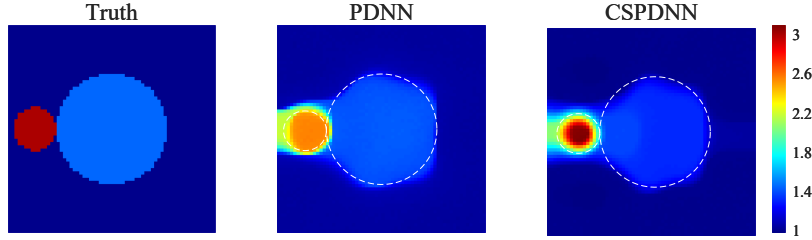


Figure 6: Imaging results based on experimental measurements “FoamDielExt”[17].

## 5 Conclusion

In this paper, a contrast-source-based physics-driven neural network (CSPDNN) is proposed for ISPs. Instead of directly estimating the relative permittivity, the neural network predicts the induced current distribution, thereby bypassing the explicit matrix inversion and significantly improving computational efficiency. Moreover, an adaptive weight updating strategy for the TV regularization term in the loss function is introduced, enabling the solver to automatically adjust to different contrast levels and noise conditions. The imaging performance of CSPDNN is extensively evaluated through representative numerical examples, including lossy and noisy scenarios, and is further validated using experimental measurements. The results demonstrate that CSPDNN achieves accurate, robust, and efficient reconstructions, highlighting its potential for practical applications.

## References

- [1] Xudong Chen. *Computational Methods for Electromagnetic Inverse Scattering*. Wiley, Hoboken, NJ, USA, 2018.
- [2] Yulong Zhou, Ning Leng, Zhun Wei, Tiantian Yin, Ming Bai, and Xudong Chen. Physics-assisted learning scheme for quantitative imaging via near-field scanning microwave microscopy. *IEEE Transactions on Microwave Theory and Techniques*, 71(7):3026–3036, 2023.
- [3] Sherif S. Ahmed. Microwave imaging in security — two decades of innovation. *IEEE Journal of Microwaves*, 1(1):191–201, 2021.
- [4] Kang An, Changyou Li, Guoqian Long, and Jun Ding. Microwave time reversal for nondestructive testing of buried small damage in composite materials. *Inverse Problems*, 40(4):045006, feb 2024.
- [5] Zhun Wei and Xudong Chen. Deep-learning schemes for full-wave nonlinear inverse scattering problems. *IEEE Transactions on Geoscience and Remote Sensing*, 57(4):1849–1860, 2019.
- [6] Lianlin Li, Long Gang Wang, Fernando L. Teixeira, Che Liu, Arye Nehorai, and Tie Jun Cui. DeepNIS: Deep neural network for nonlinear electromagnetic inverse scattering. *IEEE Transactions on Antennas and Propagation*, 67(3):1819–1825, 2019.

- [7] Zicheng Liu, Mayank Roy, Dilip K. Prasad, and Krishna Agarwal. Physics-guided loss functions improve deep learning performance in inverse scattering. *IEEE Transactions on Computational Imaging*, 8:236–245, 2022.
- [8] Yu Liu, Hao Zhao, Rencheng Song, Xudong Chen, Chang Li, and Xun Chen. SOM-Net: Unrolling the subspace-based optimization for solving full-wave inverse scattering problems. *IEEE Transactions on Geoscience and Remote Sensing*, 60:1–15, 2022.
- [9] Jie Ma, Zicheng Liu, and Yali Zong. Inverse scattering solver based on deep neural network with total variation regularization. *IEEE Antennas and Wireless Propagation Letters*, 22(10):2447–2451, 2023.
- [10] Yutong Du, Zicheng Liu, Miao Cao, Zupeng Liang, Yali Zong, and Changyou Li. Quality-factor-inspired deep neural network solver for solving inverse scattering problems. *IEEE Transactions on Geoscience and Remote Sensing*, 63:1–13, 2025.
- [11] Rencheng Song, Meilan Li, Kuiwen Xu, Chang Li, and Xun Chen. Electromagnetic inverse scattering with an untrained SOM-Net. *IEEE Transactions on Microwave Theory and Techniques*, 70(11):4980–4990, 2022.
- [12] Qian Huang, Chang Li, Xiuzhu Ye, Kuiwen Xu, and Rengcheng Song. Meta-learning-assisted untrained neural network for electromagnetic inverse scattering problems. *IEEE Transactions on Antennas and Propagation*, 73(4):2548–2560, 2025.
- [13] Yutong Du, Zicheng Liu, Bazargul Matkerim, Changyou Li, Yali Zong, Bo Qi, and Jingwei Kou. Physics-driven neural network for solving electromagnetic inverse scattering problems. *IEEE Transactions on Antennas and Propagation*, pages 1–1, 2025.
- [14] A. J. Devaney. A filtered backpropagation algorithm for diffraction tomography. *Ultrasonic Imaging*, 4(4):336–350, 1982.
- [15] M.M. Ney. Method of moments as applied to electromagnetic problems. *IEEE Transactions on Microwave Theory and Techniques*, 33(10):972–980, 1985.
- [16] W.C. Gibson. *The Method of Moments in Electromagnetics*. Chapman and Hall/CRC, New York, NY, USA, 2021.
- [17] Jean-Michel Geffrin, Pierre Sabouroux, and Christelle Eyraud. Free space experimental scattering database continuation: experimental set-up and measurement precision. *Inverse Problems*, 21(6):S117, nov 2005.